

The wild west of the Orion nebula

Alba Fernández-Martín,¹[★] William J. Henney,¹ M. Teresa García-Díaz²
and S. Jane Arthur¹

¹*Instituto de Radioastronomía y Astrofísica, UNAM, Apartado Postal 3-72, 58090 Morelia, Michoacán, México*

²*Instituto de Astronomía, UNAM, Km 103 Carretera Tijuana-Ensenada, 22860 Ensenada, Baja California, México*

Accepted XXX. Received YYY; in original form ZZZ

ABSTRACT

Key words: keyword1 – keyword2 – keyword3 – keyword4 – keyword5 – keyword6

1 INTRODUCTION

2 OBSERVATIONS AND DATA REDUCTION

2.1 Observations

High-resolution spectroscopic observations were obtained at the 2.1-m telescope of the Observatorio Astronómico Nacional San Pedro Mártir (Baja California, México) in a f/7.5 configuration using the MES-SPM instrument (Manchester Echelle Spectrometer; Meaburn et al. 2003). A total of 62 spectra were obtained from seven sets of observations carried out in 2006, 2007, 2010, 2013 and 2015. The number of positions acquired in each set of observations, dates, exposition times and airmass during the observations are summarized in Table 1.

For the 2006, 2007a, 2007b and 2010 observations the instrument was equipped with the detector SITE-3 CCD, which is an array of 1024×1024 (24μm) pixels giving a spatial resolution of 0.321 arcsec/pix (without considering the binning). On the other hand, the CDD used for the 2013a, 2013b and 2015 sets, Marconi-2, is a detector with 2048×2048 square pixel, each 13.5 μm, giving a spatial resolution of 0.176 arcsec/pix (without considering the binning). The slit width was set at 150μ (1.95 arcsec on the sky) throughout the observation and it was oriented in the north-south direction for 2006, 2007a, 2007b and 2010 observations and in the east-west direction for the 2013a, 2013b and 2015 ones.

In order to establish the exact position of the slit in each pointing we took direct slit images of short duration, in which the diffraction grating was replaced by a mirror. Additionally, thorium-argon lamp spectra were taken for wavelength calibration between each slit position.

Finally, taking the seven data sets into account, we get 56 slit-positions in H α , [N II] λ 6548 and [N II] λ 6584, lines spanning an interval of 217 arcmin in RA and 9 arcmin in DEC. In addition, exposures in [S II] λ 6717 and [S II] λ 6730

were also observed in four pointings and [O III] λ 5007 in two positions, as indicated in Table 1. In order to illustrate the spatial distribution of the observations in Fig. 1 we show the 56 slit positions observed in H α + [N II] plotted over an H α image obtained from Da Rio et al. (2009).

2.2 Data reduction

The spectra were reduced using IRAF¹ by following the standard procedure for 2D spectroscopic observations (bias subtraction, flat-fielding and cosmic ray removal). The wavelength calibration was performed using thorium-argon arcs taken between each slit position.

After transforming all the spectra to a common heliocentric velocity frame, we performed a series of further corrections to obtain well calibrated spectra in a self-consistent way.

(i) An astrometric solution was found for each of the spectra using nearby stars. This allowed us to accurately determine the slit position of each exposure.

(ii) In order to compensate the variations in the sky transparency and seeing between exposures we compare our spectra with a deep H α image of the region obtained from Da Rio et al. (2009) with the Wide Field Imager (WFI) at the 2.2-m MPG/ESO telescope at La Silla. This was done by fitting a low-order Chebyshev polynomial to the spectra to WFI profile ratio. With this we obtained a brightness normalization factor for each spectra, as well as a correction for flux gradients along the slits. The corrections are typically lower than 15 percent. This comparison also allowed us to

¹ The Image Reduction and Analysis Facility IRAF is distributed by the National Optical Astronomy Observatories, which are operated by Association of Universities for Research in Astronomy, Inc., under cooperative agreement with the National Science Foundation.

[★] E-mail: a.fernandez@crya.unam.mx

Table 1. Summary of the data set observed with the spectrograph MES-SPM.

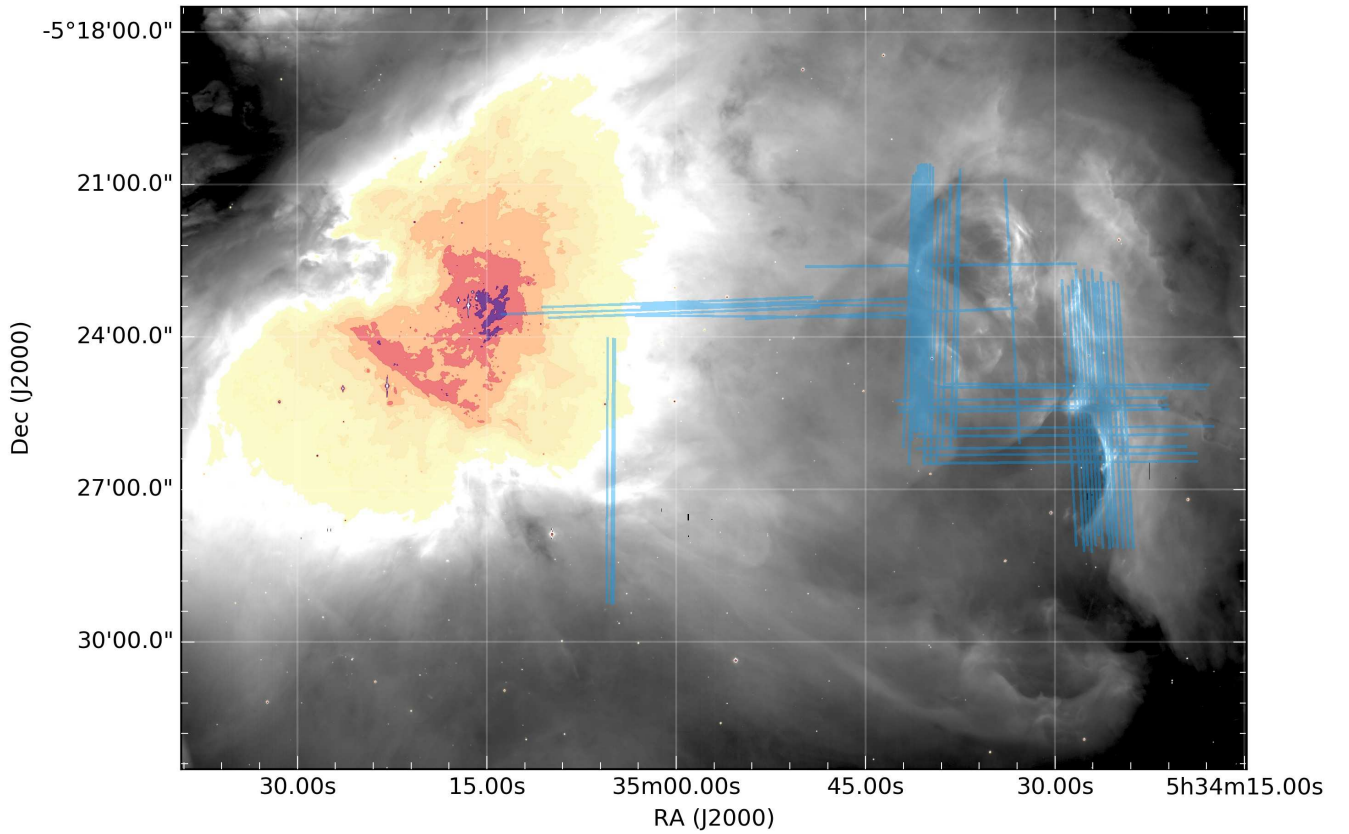
Set name	Dates	# Slits ^[a]	Orientation	Spatial resolution ^[b] (arcsec pix ⁻¹)	Cover area (arcmin ²)	Exp. time ^[c] (s)	Airmass ^[d]
2006	2006 Feb 5	11/0/0	north-south	0.624	6×6	300(3)/600(8)	1.68
2007a	2007 Jan 10	3/1/1	north-south	0.624	2×6	600	1.67
2007b	2007 Jan 13	7/0/0	north-south	0.624	14×6	600	1.30
2010	2010 Jan 15,16,17	17/3/1	north-south	0.624	17×6	450(1)/600(20)	1.37
2013a	2013 Feb 16,18,19	11/0/0	east-west	0.527	100×2	450(1)/600(10)	1.52
2013b	2013 Dec 11	5/0/0	east-west	0.527	114×0.2	600	1.49
2015	2015 Feb 3	2/0/0	east-west	0.351	88×0.2	600	1.29

^[a] Number of slit positions observed in H α + [N II] $\lambda\lambda$ 6548,6584 / [S II] $\lambda\lambda$ 6717,6731 / [O III] λ 5007.

^[b] Final spatial resolution taking the spatial binning into account.

^[c] 2006, 2010 and 2013a spectra were taken with different exposition times (separated by a bar). Number of position acquired with each exposition time are indicated in brackets. This was taking into account when combining images in the data reduction.

^[d] Mean value during the observations.

**Figure 1.** Positions and orientations of the spectroscopic settings observed in H α + [N II] with MES-SPM (in blue) plotted over the H α image of the western region of the Orion nebula obtained from [Da Rio et al. \(2009\)](#). North is up and east to the left.

flux-calibrate our spectra, using the spectrophotometry provided by [Weilbacher et al. \(2015\)](#) with MUSE in common regions.

(iii) Continuum emission was removed by fitting a two-dimensional Chebyshev function. For each exposure a background section was selected including only line-free regions of the spectrum (we use an excluded velocity window of -10 to +40 km s⁻¹ in heliocentric velocity around the line core).

In addition we use an intensity threshold to distinguish high-velocity knots from noise.

Figure 2 shows the resultant calibrated two-dimensional spectra in H α (top row) and [N II] (bottom row) for three representative slit positions.

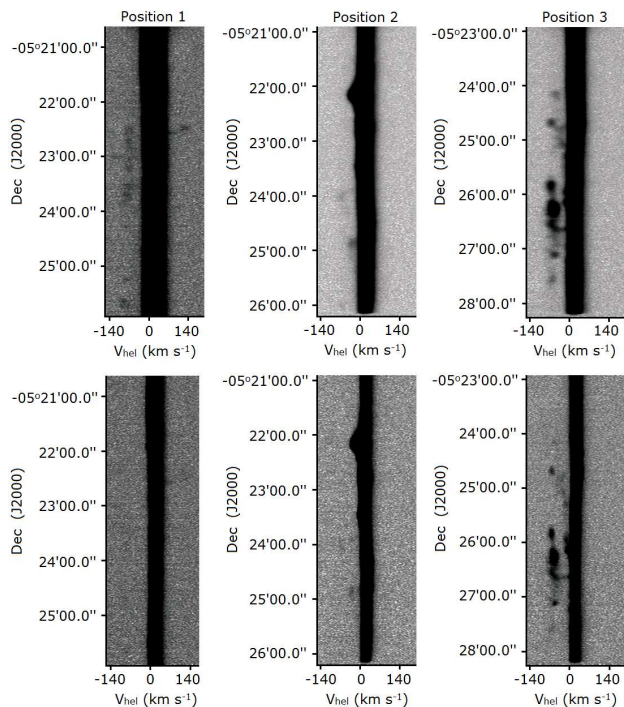


Figure 2. Calibrated two-dimensional spectra for three representative slit positions. The top row shows the $H\alpha$ emission line and the bottom one the $[N II] 6584$ emission line.

3 ISOVELOCITY MAPS

In order to better reveal the spatio-kinematical patterns in the observed region, the slit spectra were combined and interpolated to produce isovelocity channel maps. To that end, we carried out the following steps.

First, we built an orthogonal RA-DEC grid placing all the slits onto there by looping over slit profiles extracted in a given wavelength (heliocentric velocity) window. On those grid pixels in which two or more slits fall, the intensity was estimated as the mean weighted by the slit quality. Grid pixels where no slit falls were left transparent.

Due to observational The results shown in the previous section provide the velocity of the bow-shocks in our line of sight. However, to draw a tridimensional picture of the shock it is necessary to determine their velocity in the plane of the sky, i.e. to measure the proper motions.

With this aim a rough estimation of the proper motions of the large scale identified in our region was performed. We resorted to images of the western region of the Orion nebula observed with the ACS instrument of the HST which observations are separated almost 10 years. The first-epoch image was taken on April 26th 2005 while the second image was observed on March 2th 2015. The data used are calibrated and have a relative astrometric correction performed, however, to measure accurate displacements in the features we carry out an absolute astrometric calibration between both images.

We blink our matches images looking for nebular motions. In three of the five red bow shocks studied (NE, SW-S and SW-W).we find spatial displacement between the two epochs observed. In addition, we also detect clear motions

in a little arc close to the SW-W red bow sock (identified as SW-W arc). For measurement, the profiles of the shocks were traced and compared in a manual mode. The displacements of the profiles between the two epochs were then measured. Taking into account that the time passed from the first epoch to the second is 3957 days (3.10782×10^8 seconds), we derived the velocity of each shock in the plane of the sky. Results are shown in Table 3. differences between each set of observations (i.e. spatial resolution and seeing) we generated multi-resolution maps in order to not degrade the quality of the better spectra. To do that, we build several isovelocity maps onto grids with binning of 2 (better resolution), 4, 8, 16 and 32 (worst resolution).

Finally, all the grids were combined to obtain multigrid smoothed channel maps with a spatial resolution ranging from 0.5 to $15.1 \text{ arcsec pix}^{-1}$. We created maps in several velocity ranges to find kinematical structures at different velocities: the narrow band channels cover velocities from -10 to -110 km s^{-1} and from $+10$ to $+170 \text{ km s}^{-1}$ in steps of 20 km s^{-1} , while the wide bands span from $+0$ to $+60$, -60 to $+0$ and -120 to -60 km s^{-1} . The line core is also sampled in the channel ranging from -10 to $+10 \text{ km s}^{-1}$. These isovelocity maps were performed only in $H\alpha$ and $[N II]$ emission lines, because in $[S II]$ and $[O III]$ the spatial coverage of the observations is too small.

A particularly useful method of identifying large-scale velocity systems is to study images that are color-coded to simultaneously show different velocity ranges. In Fig. 3 we present combined isovelocity channel maps for $[N II]$ covering the heliocentric velocity range from -10 to $+50 \text{ km s}^{-1}$.

The analysis of the isovelocity channel maps reveal a rich harvest of results that can be subdivided into several distinct topics. In the following two sections we provide an empirical description of the kinematical features observed by using the isovelocity channel maps and the position-velocity spectra. First we describe major features seen in the western outskirts of the Orion nebula. Later we focus on blue and redshifted knots with high radial velocity.

When naming new compact objects, we have followed the convention established by O'Dell & Wen (1994) that evokes the two-dimensional position on the plane of the sky. The first four digits indicate the position of right ascension and the second three digits the position in declination (both in J2000 epoch and respect to $\alpha=5^h 33^m : XX^s . X$ $\delta=-5^\circ : 2X' : XX''$).

4 LARGE-SCALE STRUCTURES

The Western Wall is a sharp step function in the nebula surface brightness, visible as the vertically oriented bright green feature on the right hand side of Fig. 3. The southern portion of the Wall is one of the most prominent large scale features visible in direct images of the outskirts of the Orion Nebula, extending roughly 2.5 arcmin in the N-S direction from 4276-751 to 4270-544, with a slight concavity that faces East towards the Trapezium. On the East side of the Wall is a region of low $H\alpha$ surface brightness, which increases by a factor of 2-3 over a scale of $\approx 10 \text{ arcsec}$ at the position of the Wall to give a thick plateau that extends $\sim 1 \text{ arcmin}$ to the West.

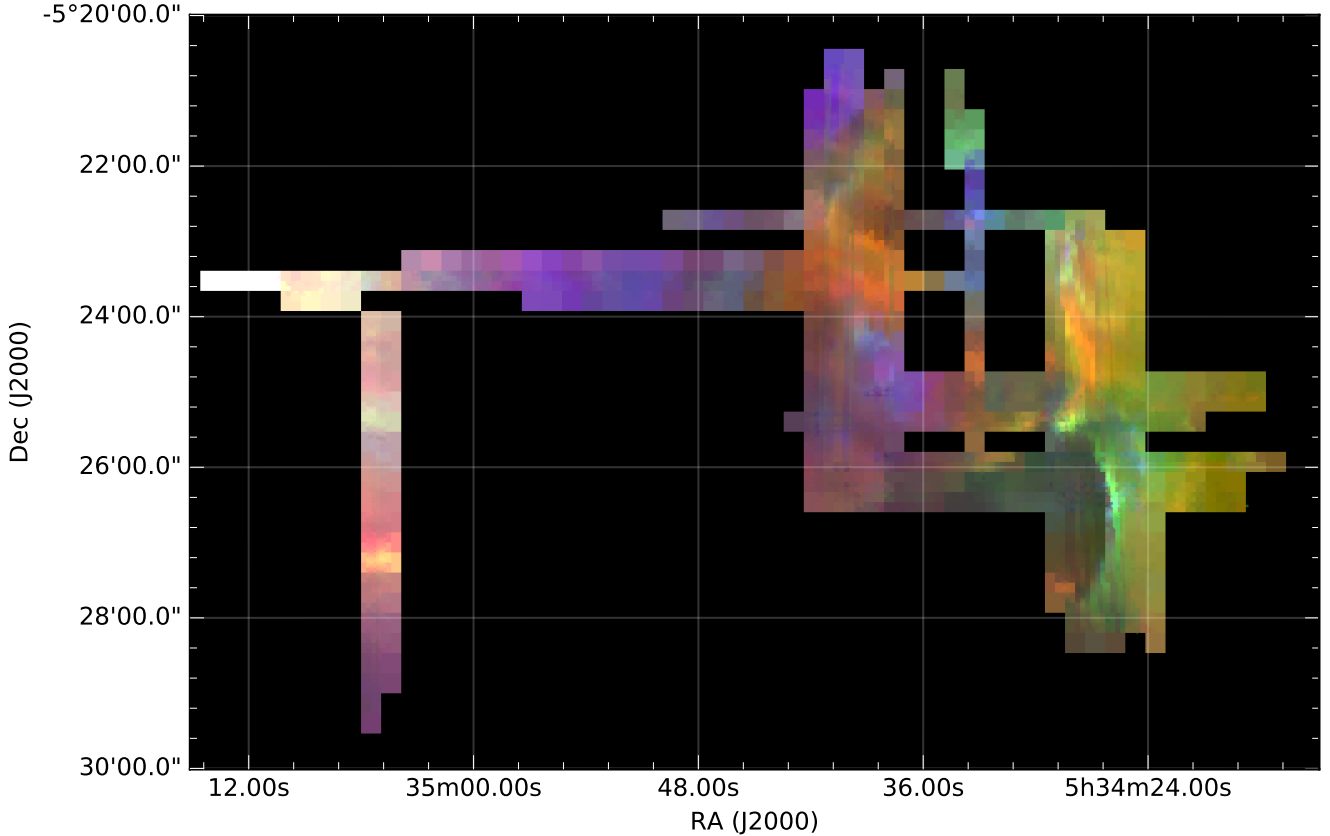


Figure 3. RGB composite image of the western region of the Orion nebula obtained from the [N II] isovelocity maps. Red corresponds to the channel maps with heliocentric velocity between +30 and +50 km s^{-1} , green between +10 and +30 km s^{-1} and blue between -10 and +10 km s^{-1} . North is up and east to the left.

Figure 4. FIGURA POR HACER (WILL): Imagen WFI con estructuras a gran escala (red bow shocks) identificadas.

At the North end of this portion of the Wall is a bright Ionized Clump of emission, centered on 4283-521 and with diameter of ≈ 10 arcsec. There are indications that the Wall extends further North than this clump, but it becomes confused with other structures superimposed on it. O'Dell et al. (2015) classified it as a shock, but it does not appear to be moving.

At least four bow-shocks lie in the western part of our observation FoV. These features show velocities slightly redshifted with respect to the systematic velocity of the nebula and their appearance is detected in both H α and [N II] isovelocity maps. The bow-shocks identified are illustrated in Fig. 4. To describe their location we use their positions relative to the Wall. In addition, in order to confirm the identification and make precise locations of the structures we resort to high spatial resolution images obtained from Da Rio et al. (2009) with the WFI (described above), Bally et al. (2006) with the Advanced Camera for Surveys (ACS) of the Hubble Space Telescope and Robberto et al. (2013) also with the ACS (hereinafter D09, B06 and R13, respectively).

The largest of the four bow-shocks is located on the northeast side of the Wall (we identified it as NE red-bow

shock). It crosses LL2, but is oriented in its opposite direction, towards the west part of the nebula. The channel maps reveal that it is moving with velocities from +0 to +50 km s^{-1} in both H α and [N II], although some regions show velocities up to 90 km s^{-1} in H α . The morphology of this bow is very well defined in the high-spatial resolution images from D09, B06 and R13, especially in B06 where it seems to be a region composed of various shocks moving toward the west.

The brighter, west-facing bow-shock we identify is located beyond the northwest of the Wall (called NW red bow-shock) and it seems to mimic the orientation of the northeast one. The bow-shock is well defined in H α , detected at velocities from +10 to +70 km s^{-1} , but is not clear in the [N II] maps, in which there are extended emission at the north of the bow-shock moving in the same range of velocities. Attending to the images, this region is spatially coincident only with the observations of D09 and R13, where it can be identified with the brighter emission of the bow-shock. However, this feature shows a less well defined bow shape than the others, as if only the edge of the paraboloid were detected. This may be because it is located close to the

boundary of the Wall, where the S/N is lower, preventing the detection the whole bow-shock.

On the western side of the Wall we identified the third red bow-shock (called SW). The composite channel maps show that it is not so redshifted as the other two presented above, moving with velocities from +10 to +50 km s⁻¹ in H α and [N II]. The bow-shock structure is clearly identifiable in the images obtained from D09 and R13 and it extends toward the southwest part of the Orion nebula. Analysing the H α images we observed that in this bow-shock it can be distinguished two orientations: the first one moving to the west (SW-W) and the second one moving to the southwest (SW-S). To check this, the kinematical study of the SW shock will be performed differentiating the two possible sub-shocks.

Finally, the isovelocity maps reveal a red bow-shock located to the southeast that is dimmer than the other features described (identified as SE). It is detected in H α and [N II] maps with velocities ranging from +10 to +50 km s⁻¹ and it crosses LL3. The structure of this bow-shock is not totally detected in the isovelocity maps because the slit positions observed do not spread enough in the southern part. Nonetheless, the whole bow morphology is perfectly identified in the H α images from D09, B06 and R13.

4.1 Kinematics of the red bow shocks

To estimate the velocity of the shocks we selected those slit positions which cross the bow-shocks in representative regions, if possible in areas close to the head of the bow. We found that no slit positions observed in [S II] or [O III] are located near the bow-shocks, so we performed this study only in H α and [N II] emission lines. One-dimensional spectra were extracted in the position of the shocks with an aperture of nine pixels. The thermal Doppler broadening of the line core (more relevant in H α than in [N II]) avoids to identify the profile of the shocks (with velocities around +20 km s⁻¹). For this reason, a subtraction of the line core was performed as a background. For each slit position we extracted one-dimensional spectra in two representative regions which were combined by a mean to sample the background variations. These regions were selected as close to perpendicular to shock as possible and in areas outside the bow-shocks to avoid that the emission of the shocked gas dominates the spectrum. Once the line core was subtracted to all the one-dimensional spectra we performed Gaussian fits to the shock profiles weighted by the uncertainties of the background. Figure 5 shows the spectral profile of one of the red bow-shocks (the northeast one) with the core subtraction and the Gaussian fit performed. All the fit performed worked well except for the NW shock where the background profile includes blueshifted emission near the line core making impossible to make a good subtraction on the blue side of the line.

Table 2 lists the properties measured for the four red bow-shocks in H α and [N II]. Each studied shock is identified in the first column. The second and third columns give the heliocentric velocities measured for the centre of the Gaussian fits. Full width at half maximum (FWHM) are presented in columns 4 and 5, while fluxes obtained from the fits are shown in columns 6 and 7. The statistical

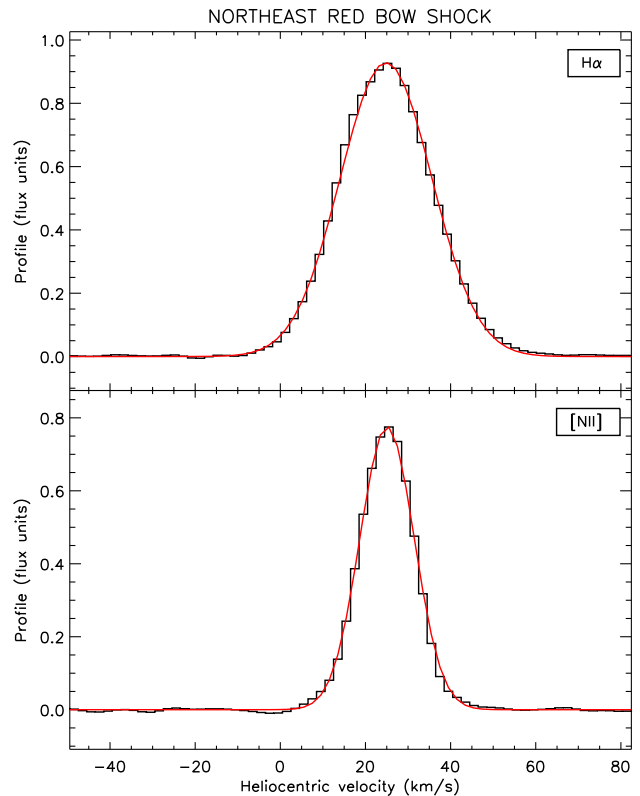


Figure 5. Spectral profiles in H α (top) and [N II] (bottom) along the line of sight of the red bow-shock located to the northeast of the Wall. The black line represents the profile extracted from the slit spectra after the core subtraction. The red line indicates the Gaussian fit performed.

Table 2. Properties of the red bow-shocks detected in the western region of the Orion nebula.

Bow-shock	V_{hel} (km s ⁻¹)		FWHM (km s ⁻¹)		Flux (Flux units)	
	H α	[N II]	H α	[N II]	H α	[N II]
NE	23.8	24.1	25.4	15.0	12.6 \pm 0.4	6.2 \pm 0.2
NW†	25.0	25.0	27.8	12.3	9.4 \pm 1.6	3.1 \pm 0.8
SE	21.9	20.6	23.9	15.7	5.0 \pm 0.3	2.3 \pm 0.2
SW-S	24.0	22.5	23.3	14.1	2.8 \pm 0.3	1.5 \pm 0.2
SW-W	21.5	20.9	25.7	17.2	13.4 \pm 0.6	9.1 \pm 0.3

† Bad subtraction of the line core.

errors associated with the measured fluxes were calculated integrating the residue of the fit over the whole velocity range of the line.

4.2 Proper motions

The results shown in the previous section provide the velocity of the bow-shocks in our line of sight. However, to draw a tridimensional picture of the shock it is necessary to de-

Table 3. Proper motions.

Bow-shock	V_x	V_y	V
NE	−82	−101	130
SW-S	−97	−102	141
SW-W	−89	−112	143
SW-W arco	−96	−94	135

termine their velocity in the plane of the sky, i.e. to measure the proper motions.

With this aim a rough estimation of the proper motions of the large scale identified in our region was performed. We resorted to images of the western region of the Orion nebula observed with the ACS instrument of the HST which observations are separated almost 10 years. The first-epoch image was taken on April 26th 2005 while the second image was observed on March 2th 2015. The data used are calibrated and have a relative astrometric correction performed, however, to measure accurate displacements in the features we carry out an absolute astrometric calibration between both images.

We blink our matches images looking for nebular motions. In three of the five red bow shocks studied (NE, SW-S and SW-W).we find spatial displacement between the two epochs observed. In addition, we also detect clear motions in a little arc close to the SW-W red bow sock (identified as SW-W arc). For measurement, the profiles of the shocks were traced and compared in a manual mode. The displacements of the profiles between the two epochs were then measured. Taking into account that the time passed from the first epoch to the second is 3957 days (3.10782×10^8 seconds), we derived the velocity of each shock in the plane of the sky. Results are shown in Table 3.

5 HIGH-VELOCITY KNOTS

Analysing the position-velocity spectra and the isovelocity maps we detect five redshifted features at high-velocities located nearby to LL1 and LL2. All of them are already catalogued by [Henney et al. \(2013\)](#) and we do not perform any study of them in this work. On the other hand, we find **147** high-velocity blueshifted features in the isovelocity maps. They are distributed over the whole observation FoV, although, as can be appreciated in Fig. 6, there is a concentration of blueshifted knots to the south-west.

Describir nuevo mġ;todo (WILL). Heliocentric velocities, FWHM and fluxes (with their corresponding errors) are presented in Table 4 for every detected blueshifted high-velocity feature in $H\alpha$ and $[N II]$.

Figure 6. FIGURA POR HACER (WILL): finding chart con knots identificados. Mejor zoom dejando 050-422 en una cajita.

Table 4: Heliocentric velocities, FWHM and fluxes for the blueshifted high-velocity knots studied in H α and [N II].

Knot	V_{hel} (km s^{-1})		FWHM (km s^{-1})		Flux (Flux units)	
	H α	[N II]	H α	[N II]	H α	[N II]
051-420	-30.00 ± 0.03	-	27.08 ± 1.58	-	9.98 ± 0.78	-
103-325	-	-32.79 ± 5.58	-	21.88 ± 8.71	-	2.49 ± 1.46
4230-523	-30.00 ± 0.54	-30.00 ± 2.43	55.14 ± 3.65	58.87 ± 5.17	2.75 ± 0.55	0.91 ± 0.09
4231-512	-30.00 ± 0.23	-35.76 ± 2.49	53.53 ± 4.30	29.62 ± 6.27	2.43 ± 0.22	0.51 ± 0.13
4240-512	-55.73 ± 2.74	-48.22 ± 2.75	18.22 ± 5.35	23.75 ± 6.87	0.43 ± 0.16	0.44 ± 0.15
4240-618	-20.00 ± 0.81	-20.00 ± 1.52	21.64 ± 4.36	58.35 ± 9.86	1.12 ± 0.27	0.93 ± 0.23
4242-635	-8.38 ± 0.32	-2.99 ± 2.55	18.24 ± 0.85	15.16 ± 2.62	4.52 ± 0.23	1.13 ± 0.24
4243-457	-17.36 ± 1.35	-20.06 ± 1.43	27.84 ± 2.34	19.34 ± 3.29	7.74 ± 2.94	2.37 ± 0.51
4243-749	-67.49 ± 1.47	-68.21 ± 0.47	25.15 ± 3.26	33.33 ± 4.80	1.40 ± 0.17	0.75 ± 0.15
4244-523	-68.02 ± 2.12	-70.75 ± 0.81	26.26 ± 3.30	19.57 ± 2.34	1.17 ± 0.29	0.26 ± 0.15
4246-556	-99.26 ± 0.57	-94.79 ± 0.30	20.37 ± 1.21	24.95 ± 0.53	0.62 ± 0.00	0.67 ± 0.04
4247-552	-66.70 ± 0.32	-66.41 ± 0.31	27.46 ± 0.78	15.00 ± 0.75	7.15 ± 0.25	3.63 ± 0.22
4248-552	-10.49 ± 1.84	-14.47 ± 0.57	28.85 ± 1.41	18.18 ± 0.70	24.46 ± 2.49	10.54 ± 0.79
4248-714	-6.06 ± 0.70	-5.04 ± 0.11	24.30 ± 1.51	11.78 ± 0.89	6.15 ± 0.39	0.47 ± 0.10
4249-657	-11.94 ± 0.46	-13.86 ± 3.42	19.54 ± 1.29	28.22 ± 7.78	2.79 ± 0.21	0.34 ± 0.17
4251-536	-70.43 ± 0.86	-70.78 ± 0.64	25.27 ± 0.84	14.86 ± 1.07	7.50 ± 1.68	2.78 ± 0.73
4251-609	-78.52 ± 1.14	-81.22 ± 0.49	28.29 ± 1.46	19.80 ± 0.32	2.74 ± 1.33	1.21 ± 0.07
4251-748	-64.85 ± 1.30	-70.12 ± 3.76	28.93 ± 2.93	39.05 ± 9.55	1.20 ± 0.15	0.85 ± 0.25
4252-514	-64.04 ± 0.15	-70.00 ± 3.47	18.79 ± 4.24	42.26 ± 7.71	0.27 ± 0.11	0.46 ± 0.18
4252-533	-8.13 ± 0.28	-9.30 ± 0.63	22.51 ± 0.69	16.22 ± 1.78	8.66 ± 0.28	1.90 ± 0.23
4252-557	-69.67 ± 0.13	-69.81 ± 0.14	25.84 ± 0.33	14.57 ± 0.40	20.20 ± 3.56	8.98 ± 1.19
4253-615	-12.54 ± 3.93	-15.79 ± 0.45	41.76 ± 2.68	26.08 ± 0.46	22.71 ± 12.37	3.96 ± 3.32
4253-653	-77.73 ± 3.26	-	20.76 ± 7.15	-	0.31 ± 0.13	-
4253-757	-58.81 ± 0.49	-60.12 ± 0.68	28.14 ± 1.31	26.61 ± 4.52	4.98 ± 1.63	2.12 ± 0.14
4254-708	-59.44 ± 0.26	-57.76 ± 0.57	16.53 ± 3.23	12.84 ± 2.10	0.34 ± 0.13	0.20 ± 0.05
4255-551	-67.91 ± 0.29	-68.98 ± 0.37	26.76 ± 0.67	17.66 ± 0.82	17.43 ± 2.73	7.46 ± 0.60
4255-610	-63.25 ± 0.53	-62.93 ± 0.50	36.80 ± 2.07	30.99 ± 0.65	10.85 ± 1.07	5.17 ± 0.02
4255-617	-95.58 ± 3.17	-100.00 ± 0.61	45.36 ± 5.84	14.94 ± 3.45	0.77 ± 0.19	0.19 ± 0.05
4255-622	-61.77 ± 0.41	-62.18 ± 0.69	41.60 ± 0.94	33.73 ± 1.11	11.11 ± 1.29	6.43 ± 1.03
4257-455	-49.83 ± 1.99	-54.75 ± 3.81	18.41 ± 0.32	24.74 ± 0.61	0.37 ± 0.08	0.32 ± 0.01
4258-626	-60.76 ± 1.02	-59.26 ± 0.19	31.73 ± 1.43	27.35 ± 0.45	15.95 ± 1.25	11.59 ± 0.23
4259-604	-14.52 ± 0.61	-14.12 ± 3.27	39.19 ± 4.25	58.87 ± 6.53	7.43 ± 0.81	2.24 ± 0.37
4259-615	-61.09 ± 1.66	-56.23 ± 1.24	33.62 ± 1.88	21.29 ± 2.77	15.94 ± 4.05	8.13 ± 1.11
4259-657	-7.04 ± 0.16	-4.92 ± 2.90	23.89 ± 0.35	34.62 ± 5.84	14.75 ± 0.22	5.64 ± 1.02
4260-649	-25.16 ± 0.19	-25.00 ± 2.45	14.79 ± 1.58	39.56 ± 15.35	0.90 ± 0.26	1.69 ± 0.75
4260-739	-61.39 ± 2.77	-63.78 ± 1.11	23.19 ± 0.02	19.65 ± 4.71	3.53 ± 0.86	1.24 ± 0.05
4261-713	-55.79 ± 1.63	-54.34 ± 2.35	27.90 ± 0.69	16.97 ± 3.79	3.13 ± 0.95	0.98 ± 0.75
4262-447	-25.30 ± 0.96	-34.51 ± 3.17	34.97 ± 6.91	17.22 ± 3.37	2.32 ± 0.72	0.59 ± 0.20
4262-512	-60.37 ± 3.45	-64.19 ± 6.22	32.42 ± 7.95	39.20 ± 16.02	0.85 ± 0.26	0.52 ± 0.25
4263-553	-61.28 ± 0.49	-61.24 ± 0.65	27.99 ± 0.24	19.15 ± 0.56	10.67 ± 0.34	3.04 ± 0.28
4263-625	-56.34 ± 0.20	-58.45 ± 0.58	32.32 ± 0.68	31.71 ± 0.92	24.06 ± 2.78	13.30 ± 1.46
4263-635	-51.60 ± 0.56	-47.17 ± 4.42	27.89 ± 0.17	19.64 ± 2.55	6.29 ± 0.60	0.18 ± 0.52
4264-459	-35.00 ± 0.62	-37.67 ± 1.99	47.41 ± 1.81	15.16 ± 8.60	4.13 ± 0.35	0.22 ± 0.23
4265-637	-12.53 ± 0.54	-15.00 ± 1.33	36.35 ± 1.77	29.91 ± 6.44	6.38 ± 0.31	1.15 ± 0.29
4265-649	-39.57 ± 0.78	-51.83 ± 1.54	58.79 ± 0.18	18.80 ± 3.59	15.30 ± 0.25	1.11 ± 0.26
4266-414	-51.84 ± 2.01	-52.96 ± 0.70	21.98 ± 1.60	15.06 ± 1.75	1.39 ± 0.60	0.27 ± 0.21
4266-553	-10.21 ± 2.06	-7.81 ± 1.02	26.43 ± 1.50	22.43 ± 2.63	11.30 ± 1.78	4.10 ± 0.30
4266-614	-51.33 ± 0.45	-54.49 ± 0.35	23.26 ± 0.72	15.87 ± 1.83	18.76 ± 2.28	5.51 ± 0.69
4267-548	-64.49 ± 0.87	-64.73 ± 0.44	27.26 ± 0.10	16.66 ± 0.05	15.18 ± 0.79	5.21 ± 0.52
4267-634	-59.22 ± 0.34	-59.03 ± 0.13	33.72 ± 1.29	27.71 ± 0.97	8.60 ± 3.02	3.41 ± 0.94
4269-610	-7.42 ± 1.76	-4.89 ± 1.11	25.67 ± 3.19	20.47 ± 0.33	13.23 ± 2.52	4.28 ± 1.21
4270-456	-15.53 ± 1.32	-26.18 ± 4.62	41.39 ± 2.30	46.35 ± 7.86	7.06 ± 0.99	1.51 ± 0.33

Continues.

Table 4: Continued.

Knot	V_{hel} (km s^{-1})		FWHM (km s^{-1})		Flux (Flux units)	
	H α	[N II]	H α	[N II]	H α	[N II]
4270-514	-9.96 ± 2.63	-9.44 ± 1.66	27.21 ± 1.79	18.90 ± 0.38	8.56 ± 1.45	1.68 ± 0.10
4270-709	-55.75 ± 1.46	-	12.68 ± 1.67	-	1.13 ± 0.27	-
4272-512	-52.99 ± 2.94	-	31.18 ± 6.05	-	1.32 ± 0.33	-
4273-547	-63.02 ± 0.59	-63.13 ± 0.33	28.72 ± 0.41	19.65 ± 0.19	10.63 ± 3.40	5.89 ± 1.71
4273-610	-62.92 ± 0.46	-65.27 ± 0.68	33.48 ± 1.82	24.07 ± 3.51	5.97 ± 0.46	1.65 ± 0.16
4274-550	-7.16 ± 2.23	-9.17 ± 0.48	24.36 ± 1.76	18.38 ± 1.00	12.76 ± 1.82	2.54 ± 0.28
4274-625	-44.56 ± 2.00	-54.57 ± 0.60	54.67 ± 1.49	23.74 ± 1.75	4.35 ± 1.31	2.09 ± 0.76
4274-711	-35.00 ± 1.38	-37.81 ± 1.13	58.84 ± 0.09	49.33 ± 10.87	3.03 ± 0.75	0.86 ± 0.01
4275-442	-60.03 ± 0.86	-62.20 ± 1.35	24.95 ± 1.14	16.19 ± 1.47	2.25 ± 0.43	0.81 ± 0.14
4275-454	-30.00 ± 0.50	-30.15 ± 1.06	57.40 ± 4.81	55.13 ± 4.75	4.66 ± 1.09	1.18 ± 0.17
4276-707	-4.99 ± 0.42	-9.60 ± 3.11	20.52 ± 0.88	21.93 ± 7.62	6.58 ± 0.29	0.52 ± 0.21
4277-528	-7.48 ± 0.35	-4.00 ± 1.48	20.49 ± 1.47	16.46 ± 1.23	10.61 ± 1.07	3.15 ± 0.33
4277-541	-76.78 ± 0.64	-77.31 ± 0.18	24.12 ± 1.44	12.60 ± 0.36	2.17 ± 0.16	0.51 ± 0.19
4279-532	-64.80 ± 0.34	-63.69 ± 1.10	13.82 ± 2.90	14.71 ± 1.85	1.29 ± 0.54	0.22 ± 0.09
4280-550	-66.73 ± 2.94	-69.84 ± 2.69	32.03 ± 1.51	20.63 ± 2.10	3.23 ± 0.65	0.84 ± 0.18
4281-258	-11.47 ± 0.70	-22.28 ± 2.39	32.59 ± 1.78	31.70 ± 0.96	7.40 ± 0.42	9.91 ± 7.90
4282-319	-12.91 ± 1.66	-24.64 ± 1.42	43.25 ± 4.53	28.04 ± 3.44	14.56 ± 12.73	3.41 ± 3.96
4283-612	-31.50 ± 1.57	-38.84 ± 1.16	48.34 ± 2.27	27.00 ± 6.75	6.17 ± 0.55	1.06 ± 0.11
4284-307	-20.18 ± 0.13	-26.21 ± 1.45	37.49 ± 1.20	27.29 ± 1.56	19.04 ± 4.90	12.55 ± 3.77
4285-316	-30.00 ± 0.01	-31.40 ± 0.13	37.33 ± 0.45	29.36 ± 0.34	26.10 ± 0.35	13.84 ± 0.19
4286-304	-12.74 ± 0.23	-5.97 ± 0.89	35.38 ± 0.79	49.44 ± 2.00	26.11 ± 0.59	17.59 ± 0.71
4286-322	-24.88 ± 1.22	-29.43 ± 0.46	35.35 ± 1.05	21.49 ± 0.97	15.13 ± 0.36	6.48 ± 0.16
4286-646	-20.00 ± 0.45	-20.00 ± 1.49	31.29 ± 4.45	29.07 ± 5.94	2.47 ± 0.40	0.78 ± 0.21
4287-441	-58.93 ± 2.60	-61.80 ± 1.00	25.49 ± 2.02	18.44 ± 1.39	1.73 ± 0.07	0.50 ± 0.20
4288-539	-67.80 ± 1.14	-67.68 ± 1.63	26.96 ± 2.77	12.33 ± 2.14	1.99 ± 0.25	0.46 ± 0.13
4288-557	-64.00 ± 0.19	-62.30 ± 0.98	24.73 ± 0.32	13.42 ± 0.16	1.30 ± 0.46	0.38 ± 0.04
4289-524	-68.81 ± 0.28	-71.27 ± 0.12	24.14 ± 1.39	15.74 ± 1.28	1.92 ± 0.32	0.40 ± 0.16
4289-556	-21.77 ± 0.94	-30.11 ± 0.38	56.23 ± 3.08	32.91 ± 2.20	8.89 ± 3.59	1.80 ± 0.23
4290-459	-7.97 ± 4.44	-8.29 ± 1.05	11.88 ± 0.61	14.46 ± 0.56	11.92 ± 1.69	4.51 ± 0.46
4290-547	-9.32 ± 0.31	-9.98 ± 0.75	26.49 ± 7.14	12.51 ± 4.23	7.09 ± 2.02	1.21 ± 0.08
4291-428	-14.75 ± 0.66	-10.00 ± 0.86	26.19 ± 1.81	37.33 ± 7.82	5.49 ± 0.43	1.81 ± 0.45
4291-547	-65.38 ± 0.83	-73.10 ± 4.01	32.91 ± 1.98	49.39 ± 13.46	2.90 ± 0.21	0.49 ± 0.23
4293-326	-13.02 ± 0.17	-	19.36 ± 0.47	-	11.04 ± 0.31	-
4294-259	-30.00 ± 0.14	-	57.92 ± 3.92	-	3.52 ± 0.33	-
4294-321	-52.54 ± 0.28	-53.29 ± 0.28	30.53 ± 0.66	21.93 ± 0.65	7.95 ± 0.21	5.13 ± 0.19
4295-603	-64.75 ± 1.05	-52.50 ± 4.95	27.28 ± 0.76	58.87 ± 11.44	0.53 ± 0.14	0.33 ± 0.10
4300-503	-7.46 ± 1.45	-6.97 ± 0.76	24.25 ± 1.34	19.55 ± 0.23	17.32 ± 4.53	3.90 ± 1.04
4301-547	-70.20 ± 1.12	-73.50 ± 1.00	32.51 ± 2.67	11.77 ± 0.66	1.21 ± 0.12	0.09 ± 0.04
4303-520	-52.44 ± 0.82	-58.53 ± 3.45	18.14 ± 2.63	16.35 ± 3.69	0.50 ± 0.06	0.12 ± 0.01
4303-526	-16.67 ± 0.46	-15.00 ± 0.55	21.43 ± 1.22	28.11 ± 4.97	2.48 ± 0.17	0.67 ± 0.14
4303-610	-35.00 ± 0.15	-	56.99 ± 6.77	-	2.55 ± 0.33	-
4305-618	-61.92 ± 3.65	-68.99 ± 3.33	19.26 ± 5.76	50.17 ± 6.83	0.35 ± 0.15	0.68 ± 0.18
4309-511	-56.74 ± 1.74	-62.79 ± 1.71	32.57 ± 2.19	45.49 ± 7.38	1.25 ± 0.23	0.34 ± 0.15
4311-547	-25.00 ± 0.02	-25.00 ± 0.45	29.83 ± 0.83	44.71 ± 9.38	5.59 ± 0.18	0.82 ± 0.21
4317-458	-12.94 ± 1.91	-9.04 ± 0.12	22.28 ± 0.75	21.31 ± 0.45	9.90 ± 2.22	2.75 ± 0.49
4318-527	-25.00 ± 0.07	-30.37 ± 1.81	41.44 ± 3.03	11.77 ± 0.93	8.13 ± 0.63	0.19 ± 0.05
4322-625	-64.67 ± 2.68	-64.84 ± 0.62	24.91 ± 0.74	15.19 ± 1.45	2.49 ± 1.38	0.83 ± 0.10
4323-522	-12.53 ± 0.46	-10.00 ± 0.16	27.13 ± 1.46	29.94 ± 3.81	9.22 ± 0.54	2.11 ± 0.29
4326-522	-63.92 ± 2.87	-	43.65 ± 11.92	-	0.55 ± 0.19	-
4328-601	-60.16 ± 3.86	-	12.90 ± 3.23	-	0.25 ± 0.13	-
4333-355	-15.25 ± 0.32	-	17.75 ± 1.79	-	2.50 ± 0.30	-
4333-403	-65.57 ± 2.29	-65.45 ± 2.60	16.85 ± 3.16	18.21 ± 5.73	0.86 ± 0.27	0.74 ± 0.29
4334-456	-15.03 ± 0.19	-15.00 ± 0.09	30.39 ± 1.42	24.17 ± 1.52	15.99 ± 2.45	3.50 ± 0.34

Continues.

Table 4: Continued.

Knot	V_{hel} (km s^{-1})		FWHM (km s^{-1})		Flux (Flux units)	
	H α	[N II]	H α	[N II]	H α	[N II]
4337-210	-	-19.53 ± 0.03	-	16.17 ± 0.07	-	56.33 ± 0.29
4338-514	-48.37 ± 5.03	-	33.71 ± 7.54	-	0.26 ± 0.14	-
4344-512	-7.43 ± 0.94	-3.46 ± 0.44	24.52 ± 1.60	17.75 ± 1.27	20.75 ± 4.43	5.40 ± 2.16
4356-525	-28.56 ± 0.35	-36.69 ± 1.04	38.07 ± 1.37	15.25 ± 0.54	8.41 ± 0.98	0.85 ± 0.17
4363-514	-35.00 ± 0.15	-44.40 ± 0.74	53.87 ± 3.83	11.92 ± 0.90	4.37 ± 0.36	0.35 ± 0.05
4368-523	-96.17 ± 7.14	-93.08 ± 4.36	18.41 ± 7.58	28.19 ± 21.34	0.10 ± 0.08	0.12 ± 0.11
4374-457	-68.60 ± 5.27	-	33.26 ± 8.40	-	0.58 ± 0.35	-
4377-210	-7.06 ± 1.85	-10.71 ± 1.80	25.36 ± 0.98	16.64 ± 3.34	21.93 ± 5.82	2.35 ± 0.62
4378-230	-60.63 ± 3.16	-	23.08 ± 7.58	-	0.49 ± 0.20	-
4378-526	-70.20 ± 0.43	-71.07 ± 1.23	31.47 ± 1.64	13.60 ± 1.80	1.35 ± 0.39	0.12 ± 0.08
4380-337	-64.21 ± 1.05	-62.95 ± 3.89	35.22 ± 2.66	16.94 ± 4.49	2.05 ± 0.19	0.29 ± 0.13
4380-343	-9.76 ± 0.32	-5.00 ± 0.82	21.48 ± 0.93	32.45 ± 3.39	5.06 ± 0.24	2.05 ± 0.24
4380-417	-81.37 ± 1.90	-87.02 ± 3.56	17.12 ± 4.53	11.77 ± 8.09	0.29 ± 0.10	0.14 ± 0.11
4380-519	-47.07 ± 2.85	-	32.75 ± 0.73	-	0.84 ± 0.36	-
4381-409	-69.19 ± 2.37	-66.01 ± 1.71	30.23 ± 7.53	18.79 ± 5.37	1.18 ± 0.69	0.18 ± 0.04
4381-438	-62.37 ± 4.57	-	18.07 ± 4.38	-	0.47 ± 0.23	-
4381-442	-	-2.30 ± 0.45	-	19.01 ± 0.75	-	6.20 ± 0.25
4381-455	-12.08 ± 0.10	1.80 ± 0.91	14.32 ± 0.27	11.77 ± 0.72	7.31 ± 0.16	4.44 ± 0.56
4381-552	-100.19 ± 1.19	-93.65 ± 1.63	21.76 ± 3.78	29.73 ± 0.57	0.24 ± 0.07	0.26 ± 0.04
4382-328	-79.75 ± 1.59	-79.79 ± 3.23	20.07 ± 1.66	12.76 ± 3.36	0.79 ± 0.55	0.31 ± 0.09
4387-223	-6.39 ± 0.85	-1.13 ± 2.26	23.01 ± 0.88	25.25 ± 5.45	17.85 ± 1.15	2.61 ± 0.63
4387-340	-63.57 ± 1.40	-66.62 ± 1.23	23.48 ± 3.50	22.53 ± 2.77	1.14 ± 0.39	0.28 ± 0.07
4389-209	-6.32 ± 0.51	-5.22 ± 0.90	21.35 ± 0.88	16.21 ± 0.41	18.99 ± 1.03	2.48 ± 0.28
4390-142	-9.61 ± 0.16	-6.06 ± 0.20	19.06 ± 0.60	15.23 ± 0.19	20.04 ± 0.41	4.39 ± 0.08
4390-326	-75.00 ± 0.89	-83.06 ± 5.34	35.60 ± 7.60	36.57 ± 10.42	0.79 ± 0.23	0.29 ± 0.17
4390-457	-71.41 ± 2.92	-	11.77 ± 13.91	-	0.09 ± 0.12	-
4391-419	-67.07 ± 5.25	-	22.68 ± 9.22	-	0.26 ± 0.14	-
4392-231	-75.20 ± 1.51	-78.11 ± 3.04	18.93 ± 1.91	12.46 ± 9.94	0.47 ± 0.11	0.15 ± 0.15
4397-356	-68.92 ± 4.18	-	20.06 ± 6.50	-	0.47 ± 0.22	-
4397-544	-88.21 ± 0.47	-89.34 ± 0.38	21.53 ± 1.11	23.09 ± 3.28	0.82 ± 0.14	0.40 ± 0.05
4398-305	-61.73 ± 2.02	-55.05 ± 2.56	11.77 ± 3.63	11.77 ± 16.60	0.23 ± 0.17	0.28 ± 0.43
4399-305	2.25 ± 0.13	3.92 ± 0.93	11.77 ± 0.05	21.99 ± 1.15	15.20 ± 0.41	4.29 ± 0.31
4399-332	-70.52 ± 0.01	-59.09 ± 6.94	18.91 ± 0.16	12.56 ± 16.02	0.70 ± 0.11	0.09 ± 0.14
4402-526	-89.98 ± 1.31	-94.12 ± 0.02	19.46 ± 1.59	25.27 ± 0.43	0.21 ± 0.08	0.18 ± 0.02
4406-246	-68.11 ± 0.80	-70.98 ± 4.43	22.16 ± 2.36	11.77 ± 3.71	1.11 ± 0.21	0.17 ± 0.03
4406-345	-71.86 ± 1.90	-76.16 ± 1.32	23.43 ± 3.11	13.46 ± 0.91	0.73 ± 0.24	0.28 ± 0.04
4406-514	-72.68 ± 5.19	-75.67 ± 3.03	31.83 ± 10.39	11.77 ± 8.92	0.55 ± 0.23	0.09 ± 0.10
4407-259	-122.94 ± 2.68	-125.00 ± 3.98	34.81 ± 10.38	56.99 ± 8.57	0.24 ± 0.06	0.64 ± 0.20
4417-354	-24.33 ± 0.65	-15.00 ± 0.28	15.55 ± 1.45	18.43 ± 4.95	1.89 ± 0.22	0.49 ± 0.16
4457-321	-68.52 ± 1.35	-75.00 ± 4.61	18.41 ± 0.46	12.30 ± 20.68	3.52 ± 1.15	1.25 ± 2.10

6 DISCUSSION

The isovelocity maps and the 2D spectra reveal many new features which have been kinematically described in the previous sections. Now, we will interpret these results to

6.1 Discussion red bow-shocks

- Decir que son los bow shocks mas grandes vistos en Orion hasta ahora.
- Edad dinamica (necesario movimientos propios).
- Tasa de perdida de masa.
- Discutir el origen de los flujos.

6.2 Blue knots classification

Estadísticas de los knots. Figuras provisionales

6.3 Jets and arcs

7 CONCLUSIONS

ACKNOWLEDGEMENTS

REFERENCES

- Baldwin, J. A., Phillips, M. M., & Terlevich, R. 1981, PASP, 93, 5
- Bally, J., Licht, D., Smith, N., & Walawender, J. 2006, AJ, 131, 473
- Da Rio, N., Robberto, M., Soderblom, D. R., et al. 2009, ApJS, 183, 261
- De Robertis, M. M., Dufour, R. J., & Hunt, R. W. 1987, J. R. Astron. Soc. Canada, 81, 195
- Henney, W. J., García-Díaz, M. T., O'Dell, C. R., & Rubin, R. H. 2013, MNRAS, 428, 691
- Meaburn, J., López, J. A., Gutiérrez, L., et al. 2003, Rev. Mex. Astron. Astrofis., 39, 185
- O'Dell, C. R., & Harris, J. A. 2010, AJ, 140, 985
- O'dell, C. R., & Wen, Z. 1994, ApJ, 436, 194
- O'Dell, C. R., Ferland, G. J., Henney, W. J., et al. 2015, AJ, 150, 108
- Robberto, M., Soderblom, D. R., Bergeron, E., et al. 2013, ApJS, 207, 10
- Shaw, R. A., & Dufour, R. J. 1995, PASP, 107, 896
- Weilbacher, P. M., Monreal-Ibero, A., Kollatschny, W., et al. 2015, A&A, 582, A114

This paper has been typeset from a $\text{\TeX}/\text{\LaTeX}$ file prepared by the author.

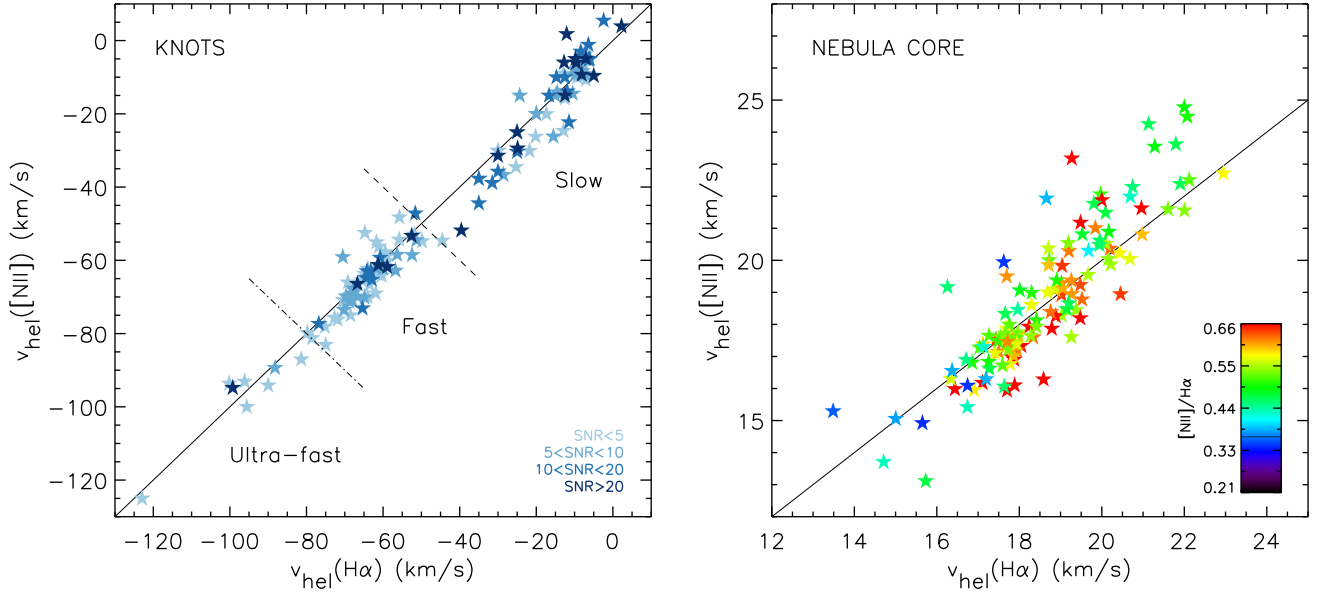


Figure 7. Estadísticas1. Provisional

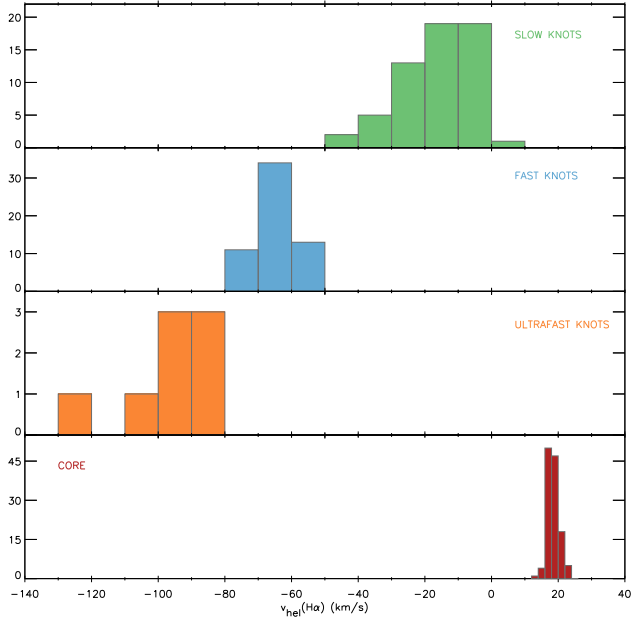


Figure 8. Estadísticas2. Provisional

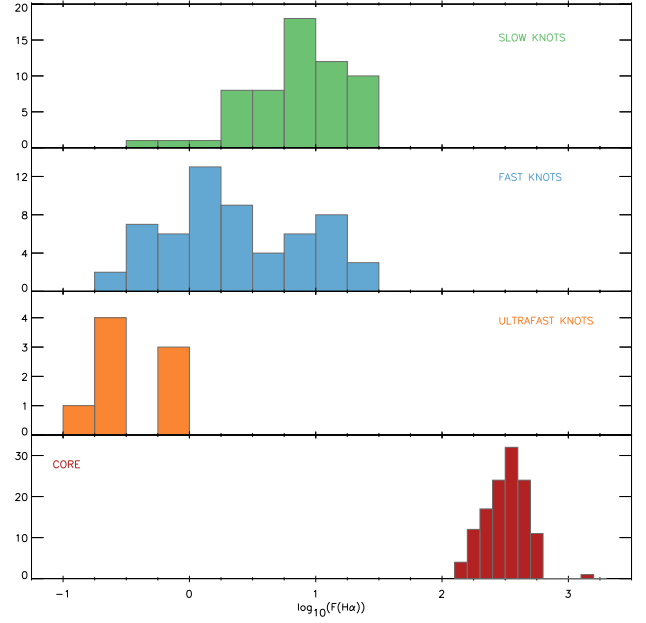


Figure 9. Estadísticas3. Provisional

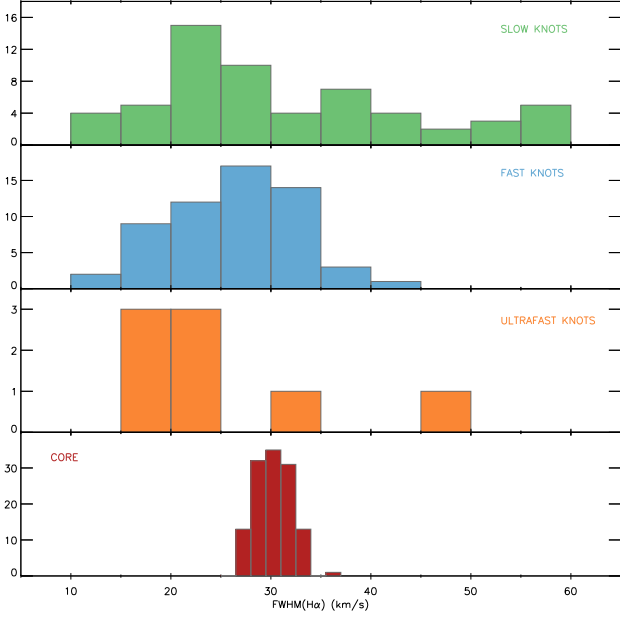


Figure 10. Estadisticas4. Provisional

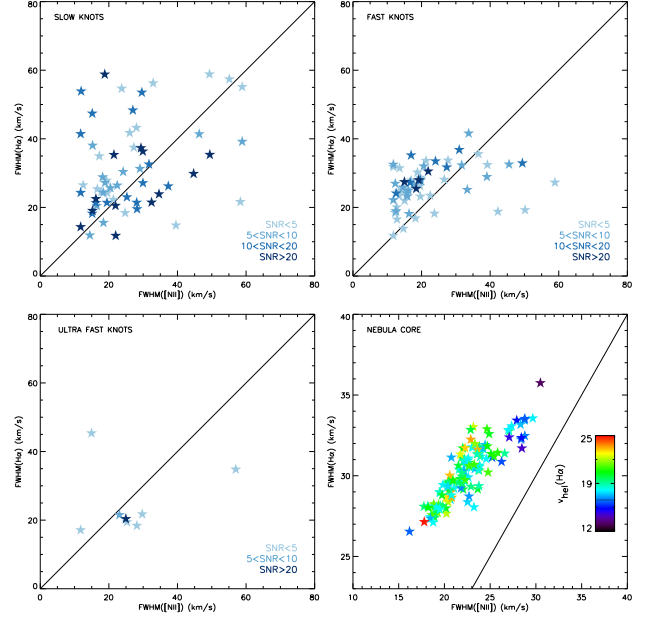


Figure 12. Estadisticas6. Provisional

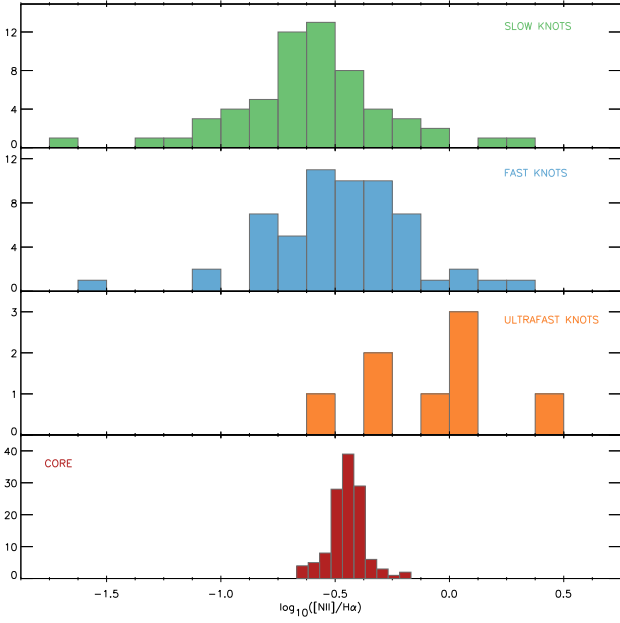


Figure 11. Estadisticas5. Provisional